Research Article

ADVANCED PHOTONICS

Spin Hamiltonian in the modulated momenta of light

Juan Feng,[a] Zengya Li,[a] Luqi Yuan,[a] Erez Hasman,[b] Bo Wang,[a,*] and Xianfeng Chen[a,c,d]

[a]Shanghai Jiao Tong University, School of Physics and Astronomy, State Key Laboratory of Photonics and Communications, Shanghai, China
[b]Technion – Israel Institute of Technology, Russell Berrie Nanotechnology Institute, and Helen Diller Quantum Center, Atomic-Scale Photonics Laboratory, Haifa, Israel
[c]Shanghai Research Center for Quantum Sciences, Shanghai, China
[d]Shandong Normal University, Collaborative Innovation Center of Light Manipulations and Applications, Jinan, China

Abstract. Spatial photonic Ising machines (SPIMs) are promising computation devices that can be used to find the ground states of different spin Hamiltonians and solve large-scale optimization problems. The photonic architecture leverages the matrix multiplexing ability of light to accelerate the computing of spin Hamiltonian via free space light transform. However, the intrinsic long-range nature of spatial light only allows for uncontrolled all-to-all spin interaction. We explore the ability to establish arbitrary spin Hamiltonian by modulating the momentum of light. Arbitrary displacement-dependent spin interactions can be computed from different momenta of light, formulating as a generalized Plancherel theorem, which allows us to implement a SPIM with a minimal optical operation (that is, a single Fourier transform) to obtain the Hamiltonian of customized spin interaction. Experimentally, we unveil the exotic magnetic phase diagram of the generalized J_1-J_2-J_3 model, shedding light on the *ab initio* magnetic states of iron chalcogenides. Moreover, we observe Berezinskii-Kosterlitz-Thouless dynamics by implementing an XY model. We open an avenue to controlling arbitrary spin interaction from the momentum space of light, offering a promising method for on-demand spin model simulation with a simple spatial light platform.

Keywords: spatial light modulator; Ising model; Plancherel theorem; machine learning; simulated annealing.

Received Mar. 20, 2025; accepted for publication Apr. 1, 2025; published online May 2, 2025.

[DOI: 10.1117/1.AP.7.4.046001]

1 Introduction

The collective behavior of numerous natural and social systems—ranging from phase transitions in matter to neural network dynamics and financial market volatility—can be described by a universal spin model that originated in physical science to study magnetism.[1] The Hamiltonian of a spin model is given by $H_r = -\sum_{ij} J_{ij}\mathbf{S}_i \cdot \mathbf{S}_j$, where J_{ij} is the interaction strength between the i'th and the j'th spin. The spin $\mathbf{S}$ is a unit vector, and J_{ij} is a function of spin-spin displacement ($\mathbf{r}_{ij}$). The spatial profile of $J(\mathbf{r}_{ij})$ plays a crucial role in determining the system's physical properties. Short-range interactions regulate critical behavior and lead to distinct phase transitions,[2] whereas long-range interactions are likely to induce correlated states for quantum entanglement. Particularly, tuning the interaction strength among several neighboring terms in $J(\mathbf{r}_{ij})$ can give rise to exotic magnetic complexity,[3,4] replica symmetry breaking,[5,6] or unusual topological effects.[7–9] Therefore, exploring spin systems of a general $J(\mathbf{r}_{ij})$ has been actively pursued both theoretically and experimentally, for the potential to unravel novel effects and to solve combinatorial optimization problems.[10]

Optical platforms offer abundant opportunities for simulating spin models via diverse light-matter interactions, such as nonlinear optical effects,[11,12] spontaneous parametric down-conversion,[13,14] lasing,[15–17] and exciton-polaritons.[18,19] A typical scheme of the optical spin model is supported by an array of resonant structures, such as coupled waveguides[20,21] or microcavities,[18,22] where the $J(\mathbf{r}_{ij})$ is realized by the field overlapping between adjacent optical modes through the leakage of evanescent fields. This strategy stands for a group of experimental efforts that aims to construct spin interactions from real-space field overlapping. However, implementing a general $J(\mathbf{r}_{ij})$

*Address all correspondence to Bo Wang, wangbo89@sjtu.edu.cn

necessitates intricate structure design and fabrication, which in turn restricts the functionality and scalability of the spin system. In addition to real-space approaches, theoretical analysis of spin models can be significantly enriched by examining the momentum spectrum of $J(\mathbf{r}_{ij})$.[23] For instance, the critical behavior of a short-range interaction corresponds to a second momentum ($\mathbf{k}^2$) in the Fourier transform of $J(\mathbf{r}_{ij})$.[24] Experimentally, the Fourier transform serves as a powerful tool in various spatial light calculations, including image processing,[25] spatial differentiation,[26–28] and convolution.[29,30]

Lately, a spatial photonic Ising machine (SPIM) has been reported as a promising optical architecture for solving large-scale spin models.[31] Leveraging the parallel processing of free space light, the optical circuit of the SPIM is well-suited for linear matrix computation with a low power consumption and high operation speed independent of the spin model scalability.[32] The proposed SPIM utilizes the central spot of the momentum space corresponding to a specific all-to-all spin interaction. Based on the primitive version, several upgraded SPIMs have utilized gauge transformation[33–35] and multiplexing techniques[36–39] to generalize the spin interaction functions. In general, the methods stemming from the central momentum of light leave the entire momentum space unexplored. Because of that, the generalization of spin Hamiltonian requires extra computational resources, which can be achieved through additional optical measurements, an increased number of wavelengths, or a larger spatial area of the spatial light modulator (SLM) chip. The required resources rely on the complexity of spin Hamiltonian. For example, for nearest-neighboring spin interaction with full-rank Hamiltonians, the required additional resource for computing the full Hamiltonian grows linearly with the number of spins.

In this work, we introduce a momentum-space-modulated spin Hamiltonian, which allows us to implement arbitrary $\mathbf{r}_{ij}$-dependent (displacement-dependent) interactions $J(\mathbf{r}_{ij})$ in a simple spatial light platform. As examples, we perform two groups of experiments to show the ability of our optical simulator. The first experiment applies a J_1-J_2-J_3 Ising spin model by tuning the interaction strength ratio among the nearest neighbor (NN), next-to-NN, and 3rd NN terms, demonstrating distinct magnetic ground states that occur in iron chalcogenides. The second experiment performs optical annealing for the XY spin model with NN interaction, exhibiting a Berezinskii-Kosterlitz-Thouless (BKT) dynamics that is governed by vortex proliferation. These experiments exhibit high calculation precision, with application potentials to solve general spin models using a simple spatial light architecture.

2 Principles and Methods

We establish a general real-and-momentum space correspondence of spin Hamiltonians (see Note 1 in the Supplementary Material for details)

$$H_k = -\sum_{ij} J(\mathbf{r}_{ij})\mathbf{S}_i \cdot \mathbf{S}_j = -\iint V(\mathbf{k}) I(\mathbf{k}) \mathrm{d}k_x\, \mathrm{d}k_y. \tag{1}$$

Here, the sum is taken over all spin pairs, including self-interactions. The modulation function $V(\mathbf{k}) \sim \sum_{ij} J(\mathbf{r}_{ij}) e^{i\mathbf{k}\cdot\mathbf{r}_{ij}}$ corresponds to the Fourier transform of $J(\mathbf{r}_{ij})$, and $I(\mathbf{k})$ is the normalized momentum-space intensity of light. The unit vector $\mathbf{S}$ is mapped to the phase of the optical field $E = \exp(i\varphi)$ via the relationship of $\mathbf{S} = (\cos\varphi, \sin\varphi)$. It results in an XY model for $\varphi \in (-\pi, \pi]$ and an Ising model for $\varphi \in \{0, \pi\}$. Equation (1) reveals a general correspondence between a two-body spin Hamiltonian and a $V(\mathbf{k})$-modulated diffraction of light. The insertion of $V(\mathbf{k})$ in the momentum space is equivalent to applying a corresponding spin interaction function $J(\mathbf{r}_{ij})$ for the real-space spins. Specifically, for $V(\mathbf{k}) = 1$, Eq. (1) reduces to the Plancherel theorem for zero spin interaction. For $V(\mathbf{k}) = \delta(\mathbf{k})$, it maps to a specific all-to-all spin interaction. Therefore, in this work, different spin Hamiltonians, such as short-range interaction, long-range interaction, and arbitrary $J(\mathbf{r}_{ij})$, can be feasibly implemented here by applying different $V(\mathbf{k})$ in the momentum space.

The experiment scheme is illustrated in Fig. 1(d). A plane wave laser impinges onto a phase-only SLM, generating a square array of optical fields with uniform amplitude and arbitrary phases. The phase of light is mapped to the in-plane spin vector in the same way as we have mentioned before [Figs. 1(a) and 1(b)]. The lens transforms the real-space light into the Fourier spectrum $I(\mathbf{k})$, which is captured by a camera (see Note 2 and Fig. S1 in the Supplementary Material). The spin Hamiltonian H_k is experimentally obtained by measuring the $V(\mathbf{k})$-weighted light intensity. Alongside the optically computed Hamiltonian, the feedback is assisted by the computer system, which generates random phases via a Markov chain,[40] and accepts new phase configurations by comparing the successively observed H_k according to the Metropolis algorithm.[41] This iterative process ensures that light evolves towards smaller H_k.

3 Results

3.1 J_1-J_2-J_3 Model Experiments

The J_1-J_2-J_3 model plays a pivotal role in revealing the intricate magnetism complexity of iron chalcogenides.[3,42,43] The Hamiltonian of J_1-J_2-J_3 model is given by $H_r = -\sum_{\mathrm{NN}} J_1 \mathbf{S}_i \cdot \mathbf{S}_j - \sum_{2\mathrm{NN}} J_2 \mathbf{S}_i \cdot \mathbf{S}_j - \sum_{3\mathrm{NN}} J_3 \mathbf{S}_i \cdot \mathbf{S}_j$. Here, the first sum is taken over all NN spin pairs, the second sum over next-to-NN spin pairs, and so on. For simplicity, we set $J_1 = -1$, and we define two parameters to describe the interaction ratios, $R_1 = J_2/J_1$, and $R_2 = J_3/J_1$, akin to the notation in Ref. 4. The theoretically calculated phase diagram for the J_1-J_2-J_3 model at $T = 0$ is depicted in Fig. 2(a).[4] Here, T is the temperature normalized by J_1/k_B. There are four types of states separated by linear boundaries determined by the interaction ratios R_1 and R_2. Among them, the antiferromagnetic ground state is the most common one that can be achieved without considering J_2 and J_3. As R_1 and R_2 increase, distinct phases emerge, such as the double-stripe pattern (4×4) and staggered-dimer pattern (4×2) [Fig. 2(b)]. These patterns are important ground-state candidates for the iron chalcogenides.

We apply the J_1-J_2-J_3 model to our simulator to solve the ground states, starting with the case of $(R_1, R_2) = (0.5, 0.9)$. The interaction function $J(\mathbf{r}_{ij})$ and the Fourier transform $V(\mathbf{k})$ are calculated and shown in Fig. 3(a), without applying periodic boundary conditions. A 10×10 random spin configuration is initially encoded onto the SLM, as depicted in Fig. 3(b). Meanwhile, the diffraction of light in the momentum space is captured by the camera. Because of the binary phase encoding for the Ising model, the diffraction in the momentum space is centrosymmetric with $I(\mathbf{k}) = I(-\mathbf{k})$. To reach the ground state without being trapped in a local minimum, we have divided the annealing process by 10 temperatures from $T = 1.8$ to $T = 0$

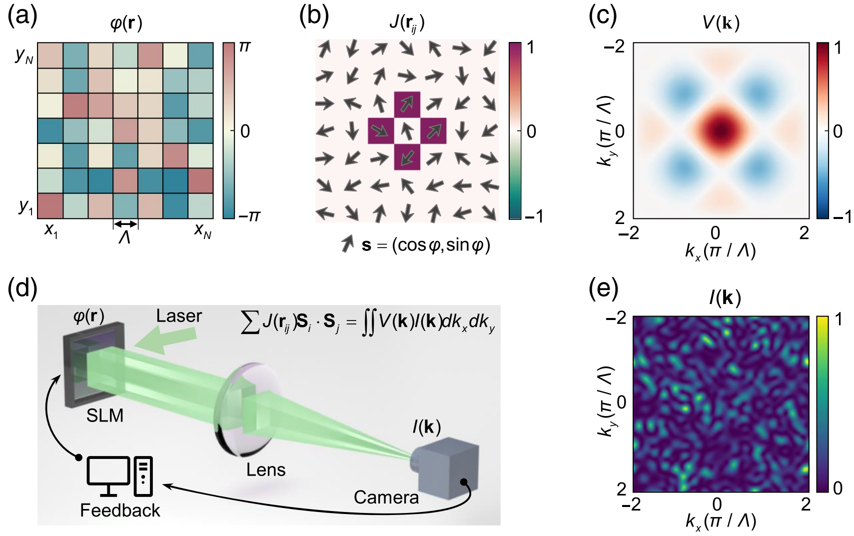

Fig. 1 Schematic of the optical spin model simulator. (a) The spin array is represented as the phases of light. The spin-lattice constant is Λ, and the size of the array is $L \times L$. (b) An example of the spin interaction function with only the NN term. The black arrows represent the XY spin vectors mapped to the phases of light. (c) The Fourier transform $V(\mathbf{k})$ of NN interaction function. (d) Simplified experimental setup. A plane wave laser beam (wavelength of 532 nm) is phase-modulated via a reflective SLM, collected by a lens, and detected by a CMOS camera in the momentum space (Fourier plane). Feedback is implemented by a computer for data processing, calculating the Hamiltonian, and updating the phase distributions. (e) An example of light momentum-space intensity distribution captured by the camera.

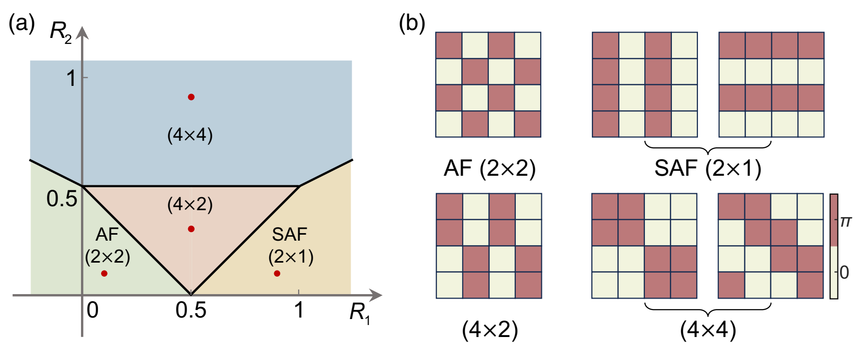

Fig. 2 Phase diagram of a J_1-J_2-J_3 model at $T = 0$. (a) The predicted phase diagram at $T = 0$ as a function of R_1 and R_2. The red dots denote the locations where we conduct experimental demonstrations. (b) The ground states correspond to the four regions in panel (a). AF, antiferromagnetic state; SAF, super-antiferromagnetic state; the notation (2×2) means that the unit cell of the ground state is composed of a 2×2 spin array. The state (4×2) is also known as the staggered-stripe pattern, (2×1) is the single-stripe pattern, and (4×4)s are the double-stripe pattern.

[Fig. 3(e)]. At every temperature, we run 2000 iterative steps to update the phase configuration to reach thermal equilibrium (see Note 4 and Figs. S8 and S9 in the Supplementary Material). During this process, the experimentally obtained H_k is depicted in Fig. 3(e). For high-T cases, the H_k is overall decreasing as the iteration continues, but it also exhibits strong fluctuation due to the simulated thermal effect from the Metropolis algorithm. At around $T \sim 1$, a minimal H_k is reached in good agreement with the theoretically predicted critical temperature in Fig. 3(f). The annealing process is terminated after 2×10^4 iterative steps and a double-stripe pattern (4×4) is observed in Fig. 3(c), which agrees with the theoretical prediction in Fig. 2(b). The momentum space intensity $I(\mathbf{k})_{\text{sol.}}$. The ground state is shown in the lower panel of Fig. 3(c), where we see four diffraction spots. During the experiment, a linear relationship between H_k and H_r is observed to verify Eq. (1), as depicted in Fig. 3(d).

Next, we systematically vary the interaction ratios R_1 and R_2 to uncover the complete phase diagram in Fig. 2. Particularly, the antiferromagnetic (AF) state [Fig. 4(a)], single-stripe [Fig. 4(d)], and double-stripe [Fig. 4(c)] are all in perfect agreement with the theoretical predictions. For $(R_1, R_2) = (0.5, 0.3)$, the solved state is slightly higher than the predicted ground state

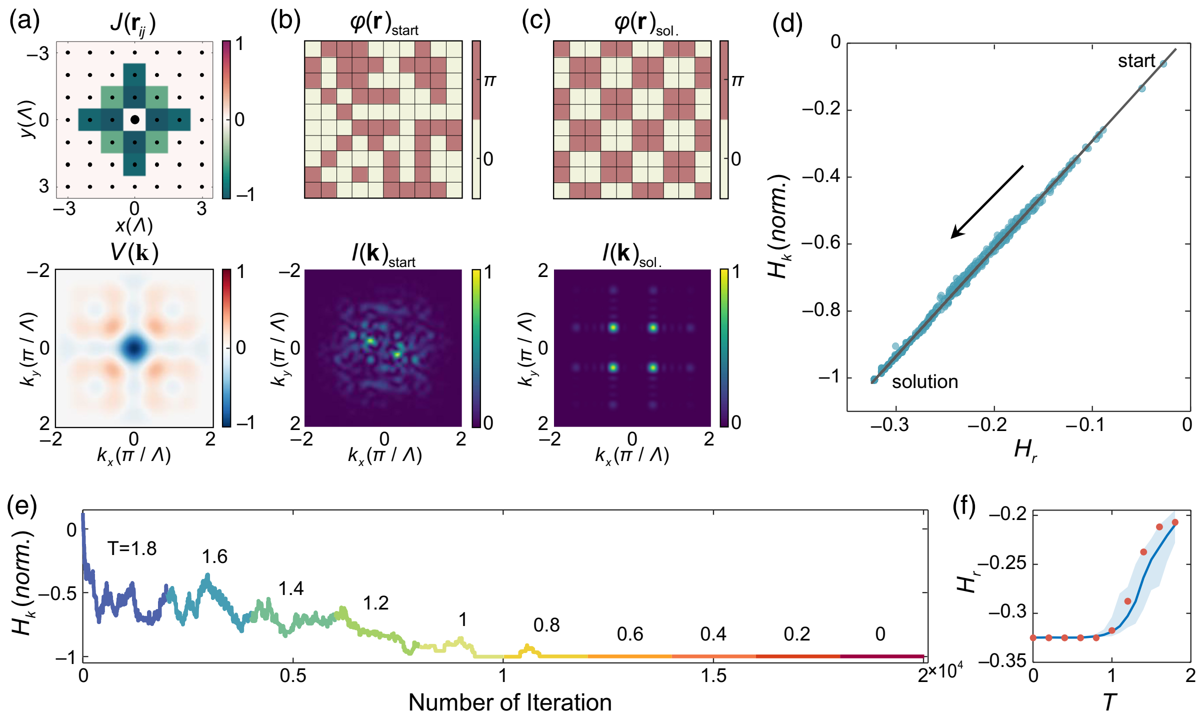

Fig. 3 Optically solving a typical ground state of the J_1-J_2-J_3 model. (a) The spin-interaction function $J(\mathbf{r}_{ij})$ for $(R_1, R_2) = (0.5, 0.9)$. The dots array stands for the locations of spins. The colormap for $J(\mathbf{r}_{ij})$ is represented by taking one of the spins at $\mathbf{r}_i = 0$. The $V(\mathbf{k})$ is the Fourier transform of $J(\mathbf{r}_{ij})$, with $V(\mathbf{k}) \sim \sum_{ij} J(\mathbf{r}_{ij}) e^{i\mathbf{k}\cdot\mathbf{r}_{ij}}$. Panels (b) and (c) are the phase distributions (upper panel) and corresponding momentum-space intensity distributions (lower panel) for an initial spin distribution (b) and the solved spin configuration (c). (d) The recorded H_r-H_k during the optical annealing (dots). All experimentally measured H_k are divided by the minimal $(-H_k)$ to obtain the normalized values. The black line is a fitted result, and the black arrow indicates the evolution direction. (e) The observed H_k during optical annealing. (f) H_r as a function of T. The dots are experimental results, the curve is the averaged simulation result, and the shaded area is the simulation variance from statistics. Note that H_r is normalized by the number of spin-spin interactions, and we have set the Boltzmann constant as $k_B = 1$.

due to the competitive interaction of the staggered-stripe pattern [Fig. 4(b)]. The newly observed state for $(R_1, R_2) = (0.5, 0.9)$ is a mixture of two cases, which is different from that in Fig. 3(c). This phenomenon arises because of the ground state degeneracy because random flips during optical annealing can stochastically choose one spin distribution over another, leading to a different or mixture of ground state configurations. From the experimental results, we can see that as $V(\mathbf{k})$ modulates the flow of light, it does not fix the spatial profile of the final $I(\mathbf{k})$. Therefore, there is no target image as proposed in Ref. 31 because the Hamiltonian is defined by a real-valued number from Eq. (1), rather than an intensity distribution. More importantly, a single target image cannot map to all ground states of a spin system, especially for a frustrated spin system that has many degenerated modes.

3.2 BKT Dynamics

We extend the use of our simulator to solve an XY model by extending the spins as quasi-continuous variables. A well-known phenomenon from the XY model is the BKT phase transition, which is a critical phenomenon characterized by the number of vortices.[44] For simplicity, we consider a ferromagnetic NN interaction that is reduced from the J_1-J_2-J_3 model by setting $J_1 = 1$ and $J_2 = J_3 = 0$. Practically, an SLM can only generate discrete phases. Therefore, we utilize a q-state clock model[45,46] to approach the XY model by dividing a continuous 2π phase into q levels. In our experiments, we encode an array (20×20) of random phases onto the SLM with $q = 8$. Typical phase distributions at different temperatures are shown in Fig. 5(a). It can be seen that the high-T system is strongly affected by thermal noise, and the phases change abruptly between neighboring spins. When the system is gradually cooling down, random phases tend to be collinear with each other by the NN spin interaction. The topological phase transition is characterized by the evolution of vortex number (N_v) as a function of T, as depicted in Fig. 5(b). The N_v crossover occurs around $T = 1$, agreeing with the numerical calculation (critical temperature $T_c \sim 0.9$). Meanwhile, we capture H_r as a function of T, as presented in Fig. 5(c). The Hamiltonian of the XY system remains at a temperature of $T \approx 0.5$, indicating the optical noise level of $q = 8$ model. In the q-clock model, the larger the value of q, the more susceptible the system is to noise. This is because, in a random process, a larger q corresponds to a smaller phase shift for each spin pixel $(2\pi/q)$, resulting in a smaller variation in relative intensity in momentum space. Notably, this noise can be reduced by using a different photodetector.

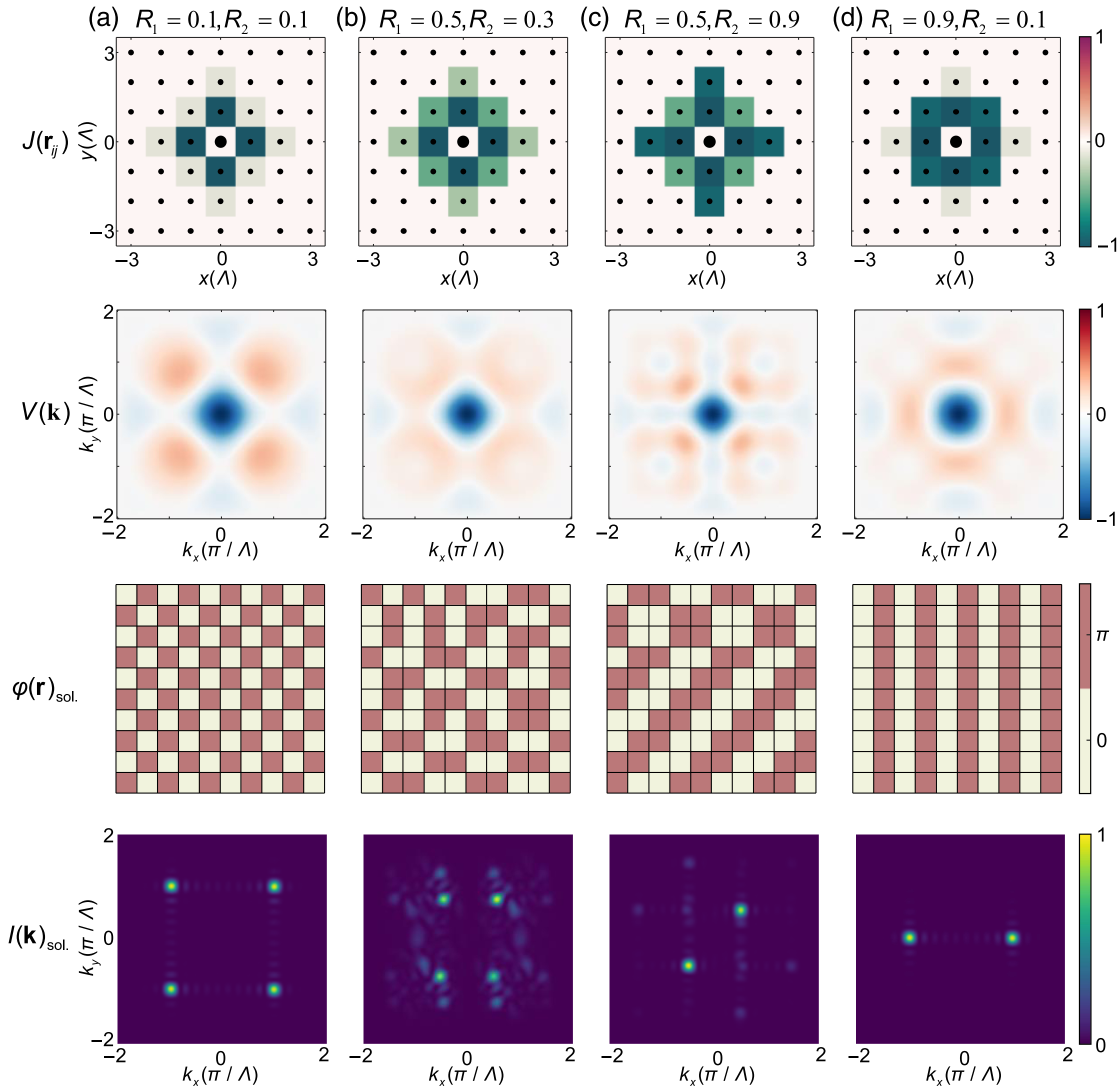

Fig. 4 Experimental demonstrations for the J_1-J_2-J_3 model phase diagram with optical momentum modulations. From the top to the bottom panels: the spin-interaction function $J(\mathbf{r}_{ij})$, the Fourier transform $V(\mathbf{k})$, the solved ground state $\varphi(\mathbf{r})_{\text{sol.}}$, and the corresponding diffraction image $I(\mathbf{k})_{\text{sol.}}$.

At last, we perform a quenching experiment to showcase the out-of-equilibrium dynamics of the XY spin system. To do that, we start with a random phase distribution and set $T = 0$. The quenching dynamics evolve through a coarsening process revealed in the H_k curve presented in Fig. 5(e)[47] (see Note 6 and Figs. S11–S14 in the Supplementary Material). The final spin configuration is trapped in a typical vortex-pair state as shown in Fig. 5(d).

4 Discussion

In summary, we have demonstrated an optical simulator to find the ground states of spin models with distinct displacement-dependent spin interactions by exploiting the momentum-space modulation of light. Although spin encoding relies on real-space optical phases, the spin interaction is governed by the modulated function $V(\mathbf{k})$ in momentum space. Remarkably, our approach allows us to extract different Hamiltonians from a single optical measurement. Compared with previous SPIMs, which inevitably increase the computing steps for complex spin interactions or complicate the optical system, our system maintains a constant computing time consumption for different spin Hamiltonian from a single Fourier transform without sacrificing the scalability of primitive SPIM.

Currently, we have utilized linear optics to demonstrate two important physical phenomena, including the complex ground states from the J_1-J_2-J_3 model, and the BKT transition from the XY model. It has been shown that a quadratic spin interaction can be realized using nonlinear optical effects,[48,49] which can be combined with our moment-space modulation method to implement a J_1-J_2-J_3-K model[3] to show the magnetism complexity of iron-based superconductors. Moreover, the implementation of an XY model is a critical step to generalize optical simulators with continuous spin variables adapting a wider group of combinatorial optimization problems. Leveraging the versatile

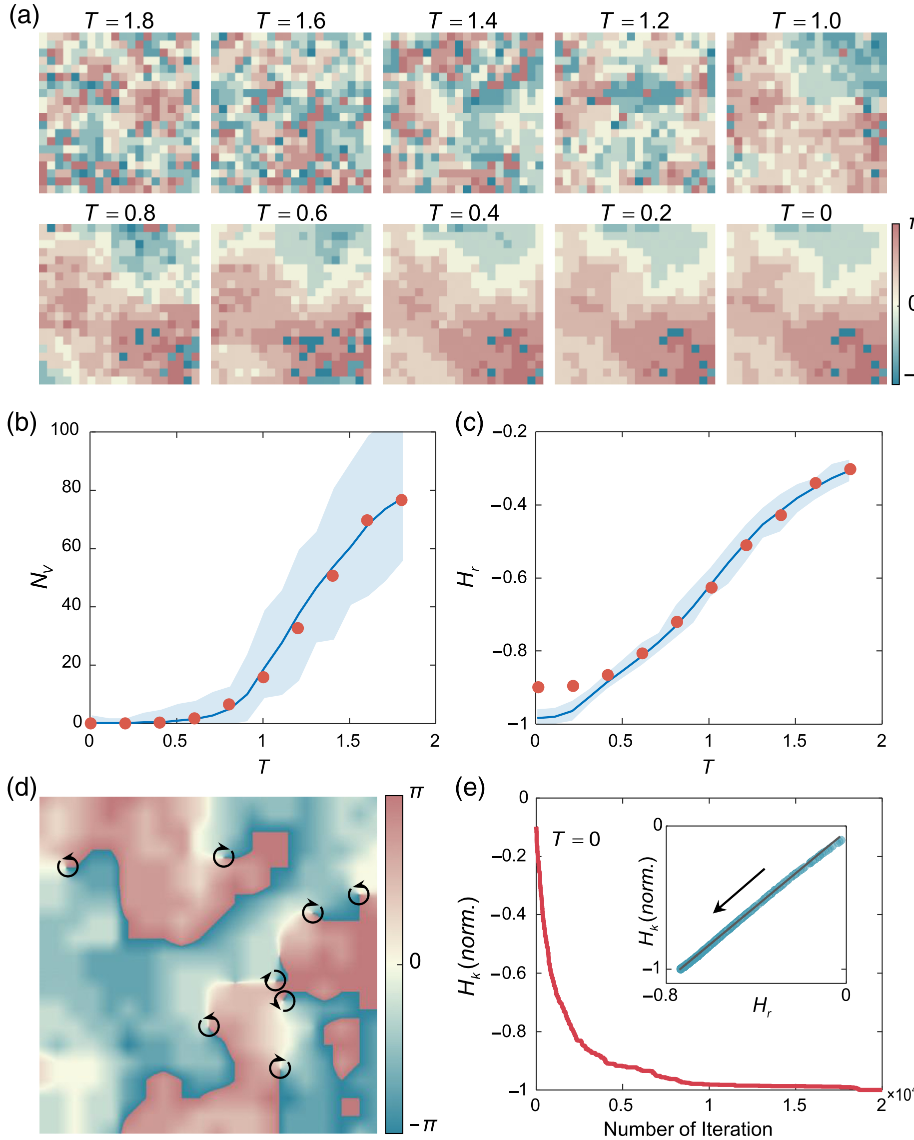

Fig. 5 Observation of BKT dynamics. (a) Observed spin distributions at different temperatures. (b) The number of vortices as a function of T. The dots are experimentally extracted from panel (a), and the curve is an averaged simulation result, with a statistical variance denoted as the shaded area. (c) Observed H_r as a function of T. (d) The observed vortex-pair state from quenching. The curved black arrows indicate the opposite signs of topological charges. (e) The experimentally recorded H_k during quenching. The inset shows the observed $H_k - H_r$ correspondence.

multiplexing technique of optics, our system can be potentially utilized to realize asymmetric or nonreciprocal interactions, such as the Dzyaloshinskii–Moriya[50,51] and Haldane interactions to simulate nontrivial topological effects. For example, we can introduce asymmetric or random spin locations onto the SLMs. This allows for the implementation of asymmetric or arbitrary spin-spin interactions J_{ij}, thereby broadening the functionality of our SPIM (Note 8 and Fig. S16 in the Supplementary Material). Moreover, the architecture of our spin model simulator is compatible with intracavity optical systems.[52–54] In this sense, $V(\mathbf{k})$ can be performed by SLMs or high-performance metasurfaces[55–58] that are placed in the momentum plane of an intracavity system with coupled lasers or exciton-polaritons. As proof-of-demonstrations, we utilized a simple annealing algorithm in this work. In the near future, optimization algorithms adapting to the SPIMs[59] and field programmable gate arrays[60] can be applied to enhance the computation performance of our simulator for better application purposes.

Disclosures

No conflicts of interest, financial or otherwise, are declared by the authors.

Code and Data Availability

The computer codes and the data that support the plots within this paper and other findings of this study are available from the corresponding author upon reasonable request.

Author Contributions

All authors have made significant contributions.

Acknowledgments

We gratefully acknowledge the financial support from the National Key Research and Development Program of China (Grant No. 2022YFA1205100), National Natural Science Foundation of China (Grant Nos. 12122407, 12192252, and 12274296), Shanghai International Cooperation Program for Science and Technology (Grant No. 22520714300), Shanghai Jiao Tong University 2030 Initiative. B.W. and L.Y are sponsored by the Yangyang Development Fund. E.H. gratefully acknowledges financial support from the Israel Science Foundation (Grant No. 1170/20).

References

1. E. Ising, "Beitrag zur Theorie des Ferromagnetismus," *Z. Physik* **31**, 253–258 (1925).
2. H. Nishimori and G. Ortiz, *Elements of Phase Transitions and Critical Phenomena*, 1st ed., Oxford University Press, Oxford (2010).
3. J. K. Glasbrenner et al., "Effect of magnetic frustration on nematicity and superconductivity in iron chalcogenides," *Nat. Phys.* **11**, 953–958 (2015).
4. D. P. Landau and K. Binder, "Phase diagrams and critical behavior of Ising square lattices with nearest-, next-nearest-, and third-nearest-neighbor couplings," *Phys. Rev. B* **31**, 5946–5953 (1985).
5. D. Pierangeli et al., "Observation of replica symmetry breaking in disordered nonlinear wave propagation," *Nat. Commun.* **8**, 1501 (2017).
6. N. Ghofraniha et al., "Experimental evidence of replica symmetry breaking in random lasers," *Nat. Commun.* **6**, 6058 (2015).
7. Y. G. N. Liu et al., "Gain-induced topological response via tailored long-range interactions," *Nat. Phys.* **17**, 704–709 (2021).
8. F. D. M. Haldane, "Model for a quantum Hall effect without Landau levels: condensed-matter realization of the 'parity anomaly'," *Phys. Rev. Lett.* **61**, 2015–2018 (1988).
9. G. Jotzu et al., "Experimental realization of the topological Haldane model with ultracold fermions," *Nature* **515**, 237–240 (2014).
10. N. Mohseni, P. L. McMahon, and T. Byrnes, "Ising machines as hardware solvers of combinatorial optimization problems," *Nat. Rev. Phys.* **4**, 363–379 (2022).
11. E. Small, R. Pugatch, and Y. Silberberg, "Berezinskii-Kosterlitz-Thouless crossover in a photonic lattice," *Phys. Rev. A* **83**, 013806 (2011).
12. G. Situ and J. W. Fleischer, "Dynamics of the Berezinskii–Kosterlitz–Thouless transition in a photon fluid," *Nat. Photonics* **14**, 517–522 (2020).
13. T. Inagaki et al., "A coherent Ising machine for 2000-node optimization problems," *Science* **354**, 603–606 (2016).
14. Z. Wang et al., "Coherent Ising machine based on degenerate optical parametric oscillators," *Phys. Rev. A* **88**, 063853 (2013).
15. M. Nixon et al., "Observing geometric frustration with thousands of coupled lasers," *Phys. Rev. Lett.* **110**, 184102 (2013).
16. M. Parto et al., "Realizing spin Hamiltonians in nanoscale active photonic lattices," *Nat. Mater.* **19**, 725–731 (2020).
17. W. Ettoumi, J. Kasparian, and J. P. Wolf, "Laser filamentation as a new phase transition universality class," *Phys. Rev. Lett.* **114**, 063903 (2015).
18. N. G. Berloff et al., "Realizing the classical XY Hamiltonian in polariton simulators," *Nat. Mater.* **16**, 1120–1126 (2017).
19. R. Tao et al., "Halide perovskites enable polaritonic XY spin Hamiltonian at room temperature," *Nat. Mater.* **21**, 761–766 (2022).
20. M. C. Rechtsman et al., "Photonic Floquet topological insulators," *Nature* **496**, 196–200 (2013).
21. Y. Shen et al., "Deep learning with coherent nanophotonic circuits," *Nat. Photonics* **11**, 441–446 (2017).
22. N. Carlon Zambon et al., "Optically controlling the emission chirality of microlasers," *Nat. Photonics* **13**, 283–288 (2019).
23. M. Suzuki, "Critical exponents for long-range interactions. II: Universality and scaling relations," *Prog. Theor. Phys.* **49**, 1106–1120 (1973).
24. D. Dantchev and J. Rudnick, "Subleading long-range interactions and violations of finite size scaling," *Eur. Phys. J. B* **21**, 251–268 (2001).
25. J. W. Goodman, *Introduction to Fourier Optics*, Roberts and Company Publishers, Greenwood Village (2005).
26. A. Silva et al., "Performing mathematical operations with metamaterials," *Science* **343**, 160–163 (2014).
27. T. Zhu et al., "Topological optical differentiator," *Nat. Commun.* **12**, 680 (2021).
28. J. Liu et al., "Intrinsic optical spatial differentiation enabled quantum dark-field microscopy," *Phys. Rev. Lett.* **128**, 193601 (2022).
29. X. Lin et al., "All-optical machine learning using diffractive deep neural networks," *Science* **361**, 1004–1008 (2018).
30. X. Meng et al., "Compact optical convolution processing unit based on multimode interference," *Nat. Commun.* **14**, 3000 (2023).
31. D. Pierangeli, G. Marcucci, and C. Conti, "Large-scale photonic Ising machine by spatial light modulation," *Phys. Rev. Lett.* **122**, 213902 (2019).
32. D. Pierangeli et al., "Scalable spin-glass optical simulator," *Phys. Rev. Appl.* **15**, 034087 (2021).
33. Y. Fang, J. Huang, and Z. Ruan, "Experimental observation of phase transitions in spatial photonic ising machine," *Phys. Rev. Lett.* **127**, 043902 (2021).
34. J. Huang, Y. Fang, and Z. Ruan, "Antiferromagnetic spatial photonic Ising machine through optoelectronic correlation computing," *Commun. Phys.* **4**, 242 (2021).
35. W. Fan et al., "Programmable photonic simulator for spin glass models," arXiv:2310.14781 (2023).
36. L. Luo et al., "Wavelength-division multiplexing optical Ising simulator enabling fully programmable spin couplings and external magnetic fields," *Sci. Adv.* **9**, eadg6238 (2023).
37. H. Yamashita et al., "Low-rank combinatorial optimization and statistical learning by spatial photonic Ising machine," *Phys. Rev. Lett.* **131**, 063801 (2023).
38. J. Ouyang et al., "On-demand photonic Ising machine with simplified Hamiltonian calculation by phase encoding and intensity detection," *Commun. Phys.* **7**, 168 (2024).
39. M. Leonetti et al., "Optical computation of a spin glass dynamics with tunable complexity," *Proc. Natl. Acad. Sci. U.S.A.* **118**, e2015207118 (2021).
40. J. R. Norris, *Markov Chains*, Cambridge University Press, Cambridge (1998).
41. N. Metropolis et al., "Equation of state calculations by fast computing machines," *J. Chem. Phys.* **21**, 1087–1092 (1953).
42. J. Colbois et al., "Partial lifting of degeneracy in the J1 - J2 - J3 Ising antiferromagnet on the Kagome lattice," *Phys. Rev. B* **106**, 174403 (2022).
43. J. Oitmaa and R. R. P. Singh, "Phase diagram of the J_1-J_2-J_3 Heisenberg model on the honeycomb lattice: a series expansion study," *Phys. Rev. B* **84**, 094424 (2011).
44. J. M. Kosterlitz, "The critical properties of the two-dimensional xy model," *J. Phys. C: Solid State Phys.* **7**, 1046–1060 (1974).
45. J. Tobochnik, "Properties of the q-state clock model for $q = 4$, 5, and 6," *Phys. Rev. B* **26**, 6201–6207 (1982).
46. Z. Li et al., "Critical properties of the two-dimensional q-state clock model," *Phys. Rev. E* **101**, 060105 (2020).
47. A. Jelić and L. F. Cugliandolo, "Quench dynamics of the 2D XY model," *J. Stat. Mech.* **2011**, P02032 (2011).

48. S. Kumar, H. Zhang, and Y. P. Huang, "Large-scale Ising emulation with four body interaction and all-to-all connections," *Commun. Phys.* **3**, 108 (2020).
49. S. Kumar et al., "Observation of distinct phase transitions in a nonlinear optical Ising machine," *Commun. Phys.* **6**, 31 (2023).
50. D. Treves and S. Alexander, "Observation of antisymmetric exchange interaction in yttrium orthoferrite," *J. Appl. Phys.* **33**, 1133–1134 (1962).
51. T. Moriya, "Anisotropic superexchange interaction and weak ferromagnetism," *Phys. Rev.* **120**, 91–98 (1960).
52. E. Maguid et al., "Topologically controlled intracavity laser modes based on Pancharatnam-Berry phase," *ACS Photonics* **5**, 1817–1821 (2018).
53. D. Naidoo et al., "Controlled generation of higher-order Poincaré sphere beams from a laser," *Nat. Photonics* **10**, 327–332 (2016).
54. M. Piccardo et al., "Vortex laser arrays with topological charge control and self-healing of defects," *Nat. Photonics* **16**, 359–365 (2022).
55. B. Wang et al., "Visible-frequency dielectric metasurfaces for multi-wavelength achromatic and highly-dispersive holograms," *Nano Lett.* **16**, 5235–5240 (2016).
56. Z. Bomzon et al., "Space-variant Pancharatnam–Berry phase optical elements with computer-generated subwavelength gratings," *Opt. Lett.* **27**, 1141–1143 (2002).
57. E. Maguid et al., "Photonic spin-controlled multifunctional shared-aperture antenna array," *Science* **352**, 1202–1206 (2016).
58. M. Khorasaninejad and F. Capasso, "Metalenses: versatile multifunctional photonic components," *Science* **358**, eaam8100 (2017).
59. C. Roques-Carmes et al., "Heuristic recurrent algorithms for photonic Ising machines," *Nat. Commun.* **11**, 249 (2020).
60. K. P. Kalinin et al., "Analog iterative machine (AIM): using light to solve quadratic optimization problems with mixed variables," arXiv:2304.12594 (2023).

Juan Feng is currently a PhD student at Shanghai Jiao Tong University (SJTU). She received her BS degree from Dalian University of Technology in 2019. Her current research interests include photonic Ising machines, spin-orbit interactions of light, and topological photonics.

Zengya Li is currently a PhD student at SJTU. He received his BS degree from the School of Physics and Microelectronics, Zhengzhou University, in 2020. His current research interests include nonlinear optics and nanophotonics.

Luqi Yuan is now a professor in the School of Physics and Astronomy at SJTU. He received his PhD in physics from Texas A&M University and was a postdoctoral scholar at Stanford University. With a focus on quantum optics and photonics, his research interests encompass a wide range of theoretical physics topics in topological photonics, non-Hermitian optics, synthetic dimensions, and hybrid quantum systems.

Erez Hasman is the Schlesinger chaired professor at the Technion – Israel Institute of Technology. He is a pioneer in the fields of optical metasurfaces, geometric-phase optical devices, and spin-optics. His current research interests include atomic-scale photonics, quantum materials, and quantum sensing and devices.

Bo Wang is an associate professor in the School of Physics and Astronomy at SJTU. He received his PhD from Peking University in 2017, and he did his 4-year postdoctoral research at the Technion – Israel Institute of Technology. His research interests include light manipulation at nanoscales, spin-orbit interactions of light, and photonic Ising machines.

Xianfeng Chen is a distinguished professor in the School of Physics and Astronomy at SJTU. He received his PhD in physics at SJTU in 1999. His current research focuses on nonlinear photonics, integrated photonics, biophotonics, and quantum information. In the past years, over 400 journal papers have been published in leading refereed journals and received more than 10,000 citations.